



Tunable Type I and II heterojunction of CoO_x nanoparticles confined in g - C_3N_4 nanotubes for photocatalytic hydrogen production

Yuxiang Zhu^a, Tao Wan^b, Xiaoming Wen^c, Dewei Chu^b, Yijiao Jiang^{a,*}

^a School of Engineering, Macquarie University, Sydney, NSW 2109, Australia

^b School of Materials Science and Engineering, UNSW Australia, Sydney, NSW 2052, Australia

^c Centre for Micro-Photonics, Swinburne University of Technology, Hawthorn, VIC 3122, Australia



ARTICLE INFO

Keywords:

Heterojunction architectures
Cobalt monoxide
Tricobalt tetraoxide
Carbon nitride nanotubes
Hydrogen production

ABSTRACT

This work reports tunable heterojunction architectures of cobalt oxides (CoO_x) nanoparticles confined on well-arrayed graphitic carbon nitride nanotubes (C_3N_4 NTs) by using a facile one-pot method but under different annealing atmospheres. A Type II heterojunction of cobalt monoxide nanoparticles (CoO NPs)/ C_3N_4 NTs was obtained after annealing under vacuum, and fine CoO NPs less than 8 nm in size were homogeneously anchored on the surface of C_3N_4 NTs. A Type I heterojunction of tricobalt tetraoxide (Co_3O_4)/ C_3N_4 NTs were formed under air condition, and Co_3O_4 NPs in the size range of 20 to 80 nm were aggregated on the surface. The photocatalytic activities of these two heterojunctions were evaluated with hydrogen production from water splitting. The strategically developed $\text{CoO}/\text{C}_3\text{N}_4$ NTs with a 7 wt. % CoO shows the highest H_2 yield under visible light irradiation and the best stability among the photocatalysts studied in this work. Comprehensive characterization results reveal that the superior performance of $\text{CoO}/\text{C}_3\text{N}_4$ NTs may be attributed to the uniformly distributed smaller nanoparticles on the well-arrayed nanotubes, the longer lifetime of excited electrons, the faster charge transfer and the stronger electronic interaction between the heterojunctions. Our Kelvin probe force microscopy results firmly verify that the $\text{CoO}/\text{C}_3\text{N}_4$ NT and $\text{Co}_3\text{O}_4/\text{C}_3\text{N}_4$ NT nanocomposites form a Type II and Type I heterojunction, respectively, and charge transfer pathways and reaction mechanisms are therefore established.

1. Introduction

Hydrogen (H_2) is potentially an ideal energy carrier, since it is environmentally benign and has the highest specific enthalpy of combustion of any chemical fuel [1]. Producing H_2 from water splitting is the most extensively studied process for storing solar energy in chemical bonds. This artificial photosynthesis requires efficient photocatalysts with proper band edge, maximum light harvesting and high stability [2]. Recently a metal-free *n*-type semiconductor, graphitic carbon nitride (g - C_3N_4), has been intensively studied and applied as visible-light active photocatalyst because of its intriguing 2D layered molecular structure and tunable band gap [3,4]. We recently reported visible-light active graphitic carbon nitride nanotubes (C_3N_4 NTs) for photocatalytic hydrogen generation even in the absence of any co-catalyst [5]. The C_3N_4 NTs show better performance than the bulk and nanosheet (NS) counterparts. Attempts are therefore being made to develop cost-effective C_3N_4 NT-based composites with improved photocatalytic activity.

Cobalt oxides (CoO_x) including cobalt monoxide (CoO) and tricobalt

tetraoxide (Co_3O_4), the earth-abundant transition metal oxides, as alternatives to precious metals, have received tremendous attention owing to their fascinating electronic and optical properties [6]. Both CoO and Co_3O_4 are nontoxic and low-cost *p*-type semiconductors. CoO has a relatively narrow band gap of around 2.6 eV which allows visible-light absorption. Nevertheless, bulk CoO was inactive in photocatalytic hydrogen production since the band positions were not suitable for water splitting. On account of quantum confinement, the edge positions of the conduction band (CB) for nanoscale CoO could be altered and become more negative than the reduction potential of H^+/H_2 . Liao et al revealed that the CB edge potential of nanostructured CoO with an average particle size of less than 10 nm rose well above the hydrogen-evolution potential compared to its micropowder counterpart. The samples exhibited a solar-to-hydrogen efficiency of 5% but became deactivated after one hour of reaction [7]. Zhan and his co-workers reported that CoO nanowires composed of assembled nanoparticles (NPs) with two different sizes (~ 34 nm and ~ 65 nm), exhibited different positions of the band edges and distinctive photocatalytic performance in H_2 generation [8].

* Corresponding author.

E-mail address: yijiao.jiang@mq.edu.au (Y. Jiang).

Nanostructured Co_3O_4 , with a direct bandgap of about 2.1 eV and comprising both Co(II) and Co(III), is thermodynamically stable under a wide range of temperatures [9]. Co_3O_4 nanomaterial is mostly used in photocatalytic oxidation owing to its excellent oxidation capacity [10]. Co_3O_4 has a larger visible-light absorption range than that of CoO owing to its narrower band gap. It was demonstrated that Co_3O_4 quantum dots were able to reduce water for H_2 production [11]. On the other hand, the CB edges for bulk CoO and Co_3O_4 are -0.11 eV and 0.37 eV; it is easier for CoO to elevate the CB minimum of the H^+ reduction potential (-0.42 eV vs NHE) [12]. Nevertheless, little work on CoO has been reported owing to its hard synthesis, which requires a special approach to force cobalt into the low valence state. Besides, CoO NPs suffer from a short lifetime, that is, after a certain irradiation they become deactivated due to corroded or oxidized surfaces. Integrating CoO NPs with other nanostructures is a promising way to overcome this shortcoming.

Strategic design of heterojunction architectures with the *n*-type and *p*-type semiconductors possessing suitable band structures, could accelerate water splitting reaction, taking into account the enhanced visible-light absorption and efficient charge separation between two semiconductors [8]. Basically, the band alignments commonly found in junction composites can be categorized into three different types (namely Type I, Type II, and Type III) [13]. Coupling of CoO_x with C_3N_4 NTs to construct heterojunction structures is a promising route to improve their photocatalytic performance. To date, *n*-type C_3N_4 has been coupled with different *p*-type semiconductors such as Cu_2O , TiO_2 , ZnO , Fe_2O_3 , Fe_3O_4 , WO_3 , CeO_2 , CoO, and Co_3O_4 to design heterojunctions for photocatalysis research [12]. Mao et al. fabricated C_3N_4 NS/CoO nanocomposites through a one-pot method applied in photocatalytic H_2 generation, nevertheless, the encased CoO NPs with large a particle size of 30–50 nm were aggregated, resulting in a loss of 17 % activity up to 3 recyclings [14]. Guo et al. synthesized $\text{CoO}/\text{C}_3\text{N}_4$ NSs through a solvothermal method for overall water splitting under visible light irradiation (> 400 nm), showing high stability of the sample containing 30 wt. % of CoO in the range of 10–20 nm [15]. On the other hand, $\text{Co}_3\text{O}_4/\text{C}_3\text{N}_4$ heterojunctions were reported for photocatalytic water oxidation [16] and methyl orange degradation [17].

The structural property and energy band profile of semiconductor heterojunctions depend largely on their synthesis procedures. This work presents tunable heterojunction architectures of CoO_x nanoparticles confined on well-arrayed C_3N_4 NTs by using the same one-pot method after annealing under vacuum or static air atmosphere. The resulting $\text{CoO}/\text{C}_3\text{N}_4$ NT (Type II) and $\text{Co}_3\text{O}_4/\text{C}_3\text{N}_4$ NT (Type I) heterojunctions exhibited distinct photocatalytic activity and stability in hydrogen production under visible-light irradiation. Comparative studies on the morphological and structural properties, band positions, electron lifetimes, and charge transfer pathways were undertaken by various characterization techniques. Finally, the charge transfer pathways and reaction mechanisms are established and evidenced by Kelvin probe force microscopy. This research presents a new strategy to tune Type I and Type II heterojunction architectures of two semiconductors. The results demonstrate the potential widespread utility of this method for developing cost-effective photocatalysts using metal oxides that are abundant in nature.

2. Experimental section

2.1. Catalyst fabrication

C_3N_4 NTs were prepared by a modified process according to the literature [18]. As shown in Fig. S1 (Supporting Information), firstly, 5 g melamine and 30 mL water were placed into a crucible under ultrasonication for 15 min. It was heated at 80 °C to achieve a moderately compact packing degree and then the floating part was removed. Secondly, the crucible was heated up to 500 °C for 2 h with a heating rate of 10 °C min⁻¹, then the temperature was increased to 550 °C at a

heating rate of 2 °C min⁻¹, and kept for another 2 h. Finally, the obtained products were ground into fine powders for future use.

CoO_x were decorated on C_3N_4 NTs via a one-pot method that is a single binder-free, low-cost process [14]. 0.5 g of C_3N_4 NT powder was dispersed in 50 mL of ethanol and stirred for 1 h, followed by adding a nominal amount of cobalt acetate. Then the solution was stirred overnight and dried at 80 °C for 1 h. Finally, the dried powder was annealed at 400 °C for 4 h with a heating rate of 10 °C min⁻¹ under vacuum, leading to $\text{CoO}/\text{C}_3\text{N}_4$ NT composites, or in a static air atmosphere to form $\text{Co}_3\text{O}_4/\text{C}_3\text{N}_4$ NTs, and then naturally cooled to room temperature. Samples are designed as $\text{CoO}(x)/\text{C}_3\text{N}_4$ NTs or $\text{Co}_3\text{O}_4(y)/\text{C}_3\text{N}_4$ NTs, where x and y denote the CoO or Co_3O_4 content in wt. %, respectively. For comparison, CoO and Co_3O_4 NPs were fabricated through the same procedure but without adding C_3N_4 NTs.

2.2. Characterization

X-ray diffraction (XRD) analysis was performed using a PANalytical X'Pert PRO diffractometer via $\text{Cu K}_{\alpha 1}$ radiation. Field emission scanning electron microscopy (FE-SEM) images were obtained by a JEOL-7100 F microscope operating at a voltage of 5 kV. Elemental analysis was conducted on a Phenom XL scanning electron microscope with an energy dispersive X-ray spectrometer (EDS). High-resolution transmission electron microscopy (HRTEM) images and selected area electron diffraction (SAED) were recorded using a JEOL-2100 F microscope operating at 200 kV. X-ray photoelectron spectroscopy (XPS) was recorded on an ESCALAB 250Xi spectrometer (Thermo Scientific, U.K.).

Ultraviolet-visible (UV-vis) diffuse reflectance spectra were obtained on a Cary 5000 spectrophotometer using BaSO_4 as the reference. The steady-state photoluminescence (PL) spectra were recorded on a Fluorolog-Tau3 fluorescence spectrophotometer with an excitation wavelength of 330 nm. Time-resolved PL was measured using the time correlated single photon counting (TCSPC) technique on an MT200 microscope (Picoquant). A 405 nm laser with a pulse repetition rate of 10 MHz was applied as excitation and the signal was detected by a single photon avalanche photodiode (APD) through a 460/40 nm bandpass filter. The decay curves were fitted by the double-exponential decay function $y = A_1 \exp(-t/\tau_1) + A_2 \exp(-t/\tau_2)$ and the average lifetime was obtained by $\tau_{AV} = (A_1 \tau_1^2 + A_2 \tau_2^2) / (A_1 \tau_1^2 + A_2 \tau_2^2)$. The photocurrent measurements were performed on a potentiostat (SP-300, BioLogic Science Instruments) using a three-electrode setup with a Pt wire as the counter electrode, the Ag/AgCl electrode (saturated KCl) as the reference electrode and the prepared catalyst/Ti sheet as the working electrode. The electrolyte was a 0.1 M Na_2SO_4 aqueous solution. Transient photocurrent responses were carried out as light on and off at a constant potential of +0.1 V, and a 300 W Xenon arc lamp (LX300, Peccell Technologies, Inc.) was employed as the light source.

Kelvin probe force microscopy (KPFM) was performed at ambient conditions using a Bruker Dimension ICON SPM with a Pt-coated probe. The surface potential difference between the sample and the probe was measured with a tip lift height of 30 nm. The probe-sample distance was precisely controlled by the software of Kelvin probe system. The powder sample dispersed in Milli-Q water was spin-coated on a silicon wafer that was previously cleaned with ethanol and dried by N_2 gas. The obtained sample was dried for 24 h prior to the KPFM measurements. The potential results were analyzed by the software NanoScope Analysis.

2.3. Photocatalytic hydrogen production

Visible-light irradiation was obtained from a 300 W Xenon arc lamp by removing the UV irradiation with a 420 nm cut-off filter. In a typical procedure, 40 mg of the prepared catalysts and 40 mL of triethylamine (TEA)/water mixture in a volume ratio of 1:9 were poured into a quartz reactor. Subsequently, argon gas was purged into the system for 15 min to completely vent out the air and it was then evacuated for another

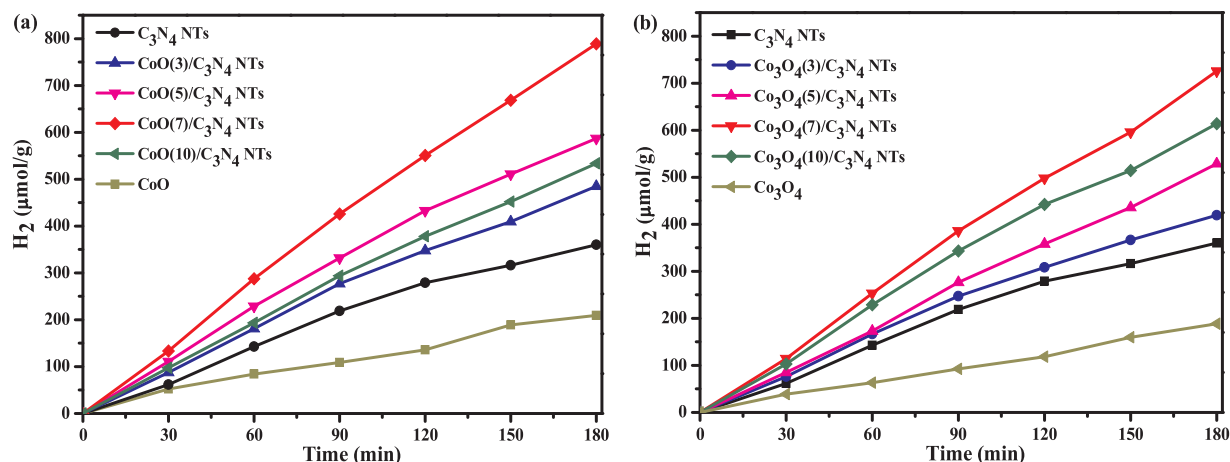


Fig. 1. H₂ generation over C₃N₄ NTs loaded with different content of CoO (a) and Co₃O₄ NPs (b) under visible light irradiation. Reaction condition: 40 mg catalyst in 40 mL water/TEA solution (volume ratio of 9/1) and visible light irradiation (> 420 nm) for 3 h.

15 min. After that, the mixture was irradiated from the top with the lamp under stirring, and a water jacket was placed to absorb the heat. The resulting gas was analyzed every 30 min using a chromatograph (GC 2014; Shimadzu Corporation) equipped with a thermal conductivity detector.

3. Results and discussion

3.1. Photocatalytic performance

As shown in Fig. 1a the photocatalytic performance of bare CoO and C₃N₄ NTs decorated with different CoO content from 3 to 10 wt. % were investigated for photocatalytic H₂ generation from water splitting under visible-light irradiation. CoO NPs yielded 209.6 μmol/g of H₂ within 3 h, lower than the bare C₃N₄ NTs (360.0 μmol/g). The activities of all CoO/C₃N₄ NT heterojunctions are higher than that of the bare C₃N₄ NTs. In detail, after 3 h illumination H₂ yields over the CoO/C₃N₄ NTs composites with 3, 5, 7 and 10 wt. % of CoO content correspond to be 484.9, 587.1, 788.6 and 533.5 μmol/g, respectively. It is noted that the rate of H₂ evolution over the CoO(7)/C₃N₄ NT sample is almost 2.2 times as high as that of the bare C₃N₄ NTs. A lower H₂ evolution was observed when the CoO loading was increased further (CoO(10)/C₃N₄ NTs), which may be attributed to the decoration of excessive CoO leading to larger CoO particles and a considerable amount of C₃N₄ NT surface active sites inaccessible to the light and the reactants. Fig. 1b shows the H₂ evolution profile of the Co₃O₄/C₃N₄ NT composites with different Co₃O₄ content (3, 5, 7 and 10 wt. %). Among them, the Co₃O₄(7)/C₃N₄ NT catalyst exhibits the highest amount of H₂ generation (725.7 μmol/g) which is about twice that of C₃N₄ NTs. Notably, the activity is lower than that of CoO(7)/C₃N₄ NTs. The AQE of CoO(7)/C₃N₄ NTs, Co₃O₄(7)/C₃N₄ NTs, and C₃N₄ NTs is determined to be 4.928, 4.077, 2.209%, respectively. The AQE of 1.9% for the CoO/C₃N₄ was reported at the 420 nm wavelength. However, the transmittance was not provided for comparison [15]. In contrast, the photocatalytic performance of CoO and Co₃O₄ NPs were also evaluated. It can be seen that Co₃O₄ NPs resulted in a lower H₂ evolution rate than CoO NPs.

The stability of the CoO(7)/C₃N₄ NT and Co₃O₄(7)/C₃N₄ NT photocatalysts was investigated after they were recovered from the reaction mixture and reused for another fresh solution. As shown in Fig. 2, good photocatalytic performance of CoO(7)/C₃N₄ NTs was maintained for at least four cycling runs, only losing 6.0%. However, the Co₃O₄(7)/C₃N₄ NT nanostructure lost almost 18.0% of the H₂ yield. It is apparent that CoO(7)/C₃N₄ NTs exhibit much better stability than that of Co₃O₄(7)/C₃N₄ NTs. In the next sections, CoO(7)/C₃N₄ NTs, Co₃O₄(7)/C₃N₄ NTs, bare C₃N₄ NTs, CoO and Co₃O₄ NPs were selected for further investigations.

3.2. Structure characterization

Fig. 3 shows the XRD patterns for CoO(7)/C₃N₄ NTs, Co₃O₄(7)/C₃N₄ NTs, bare C₃N₄ NTs, CoO and Co₃O₄ NPs. The bare C₃N₄ NTs reveal two XRD peaks at $2\theta = 13.0^\circ$ and 27.4° . The former is indexed as the (100) diffraction of graphitic C₃N₄ and can be related to an in-plane structural packing motif, whereas the latter is due to the (002) plane with characteristic interlayer stacking of conjugated aromatic systems [19,20]. These two diffraction peaks are also observed for both CoO(7)/C₃N₄ NT and Co₃O₄(7)/C₃N₄ NT samples indicating that the typical structure of graphitic C₃N₄ did not alter upon surface modification with cobalt oxides. For CoO NPs, the peaks at 36.5, 42.4, 61.5, 73.7 and 77.5° can be assigned to the (111), (200), (220), (311) and (222) facets of cubic CoO, respectively (JCPDS no. 48-1719) [21,22]. The XRD profile of CoO(7)/C₃N₄ NTs shows the same characteristic humps of CoO NPs, which verifies the presence of CoO NPs on the C₃N₄ NTs.

The XRD patterns of Co₃O₄ NPs demonstrate that they are face-centered cubic phase (JCPDS no. 42-1467) [23]. Except for the typical peaks of graphitic C₃N₄ in the XRD profile of Co₃O₄/C₃N₄ NT nanocomposites, the Co₃O₄ NP crystal planes are clearly observed, indicating the success of Co₃O₄ deposition on the C₃N₄ NTs. Furthermore, we examined the crystal structures of CoO(7)/C₃N₄ NTs and Co₃O₄(7)/C₃N₄ NTs before and after recycling experiments by XRD analysis (Fig. S2, Supporting Information). No significant change in their patterns is observed, which confirms that CoO/C₃N₄ NTs and Co₃O₄/C₃N₄ NTs are stable and reusable photocatalysts. Furthermore, from the enlarged patterns in the inset, the slightly decreased intensity of the main peaks indexed to Co₃O₄ NPs was detected, implying a tiny portion of Co₃O₄ NPs deposited on the surface of C₃N₄ NTs may be lost during the recycling process due to the relatively larger Co₃O₄ particle size and lower binding force between Co₃O₄ and C₃N₄ support. This explains the relatively lower stability of Co₃O₄/C₃N₄ NT catalyst.

The as-synthesized bare C₃N₄ NT materials exhibit tube-like morphology with an average diameter of about 80 nm as seen in the FE-SEM and TEM images (Fig. S3, Supporting Information). The nanotubes are well arranged in a compact ordered array and some are even longer than 10 μm. The elemental mapping of CoO(7)/C₃N₄ NTs and Co₃O₄(7)/C₃N₄ NTs determined by SEM-EDS in Fig. S4 (Supporting Information) reveals the homogenous distribution of cobalt, oxygen, and nitrogen elements in the nanostructures. The atomic and weight ratios of Co, O, C and N are summarized in the inset tables. The atomic ratios of Co/N determined from SEM-EDS resembles the nominal content of CoO and Co₃O₄, which further confirms that CoO and Co₃O₄ NPs were successfully deposited on the surface of C₃N₄ NTs.

High-resolution TEM and SAED were employed to investigate the microstructure of CoO and Co₃O₄ NP deposited samples. Fig. 4a–c show

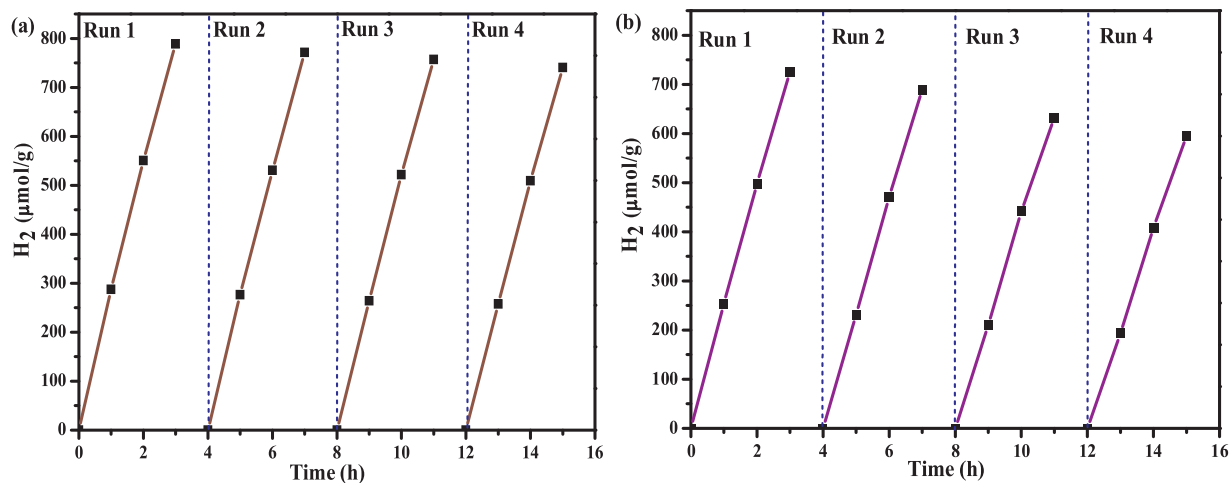


Fig. 2. Cycling runs for H₂ evolution over CoO(7)/C₃N₄ NTs (a) and Co₃O₄(7)/C₃N₄ NTs (b). Reaction condition: 40 mg catalyst in 40 mL water/TEA solution (volume ratio of 9/1) and visible light irradiation (> 420 nm) for 3 h.

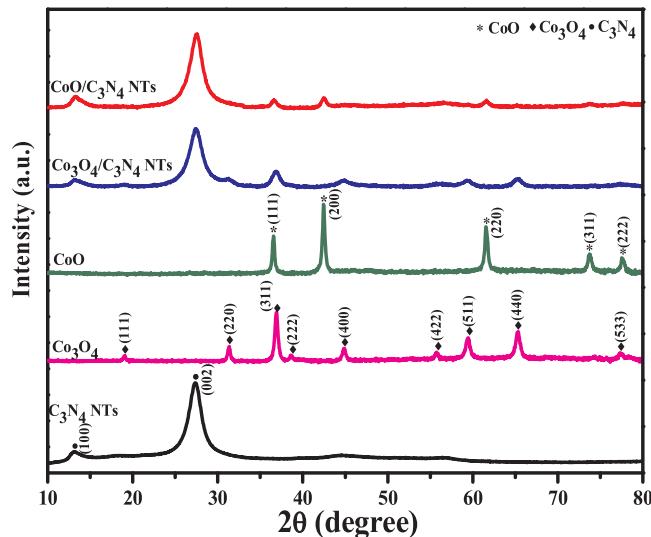


Fig. 3. XRD patterns of C₃N₄ NTs, Co₃O₄, CoO, CoO(7)/C₃N₄ NTs and Co₃O₄(7)/C₃N₄ NTs.

the TEM images of CoO(7)/C₃N₄ NTs. From the low-magnification image (Fig. 4a), well-distributed CoO NPs are observed on the surface of the C₃N₄ NTs. The high-resolution TEM images in Fig. 4b demonstrate that the CoO NPs, with a uniform particle size of around 8 nm, are tightly anchored on the well-defined C₃N₄ framework, illustrating the existence of an interface between CoO and C₃N₄ NTs. Lattice spacings of 0.213, 0.246 and 0.151 nm were determined and assigned to the (200), (111) and (220) planes of CoO crystals, respectively. The diffraction rings of the SAED pattern in Fig. 4c reveal the cubic lattice structure of CoO NPs [7], corroborating well with the previous XRD results. Fig. 4d–f show the TEM images of Co₃O₄(7)/C₃N₄ NT nanocomposites. In Fig. 4d it is found that Co₃O₄ NPs with the particle size from 10 to 50 nm, were deposited with a certain aggregation on the surface of the nanotubes. This can explain the poor activity and stability of Co₃O₄(7)/C₃N₄ NTs in H₂ generation compared with the CoO(7)/C₃N₄ NT sample. The lattice fringe (Fig. 4e), allows the identification of crystallographic spacings of $d = 0.202$, 0.244 and 0.142 nm matching well with the (400), (311) and (440) planes of Co₃O₄ NPs. In the SAED patterns (Fig. 4f) the three planes are observed, further demonstrating the cubic structure of Co₃O₄ [23]. TEM images of CoO(10)/C₃N₄ NTs and Co₃O₄(10)/C₃N₄ NTs were shown in Fig. S5a–b. For comparison, the particle sizes of the bare CoO and Co₃O₄ NPs were determined to be

approximately 10 nm and 20–80 nm, respectively (see Fig. S5c–d, Supporting Information).

Fig. 5 shows the UV-vis diffuse reflectance spectra (DRS) of the bare C₃N₄ NTs, CoO(7)/C₃N₄ NTs, Co₃O₄(7)/C₃N₄ NTs, CoO and Co₃O₄ NPs. The spectrum of the bare C₃N₄ NTs presents a steep absorption edge at near 460 nm. The band gap of C₃N₄ NTs (Fig. 5b) was determined to be around 2.74 eV by applying the Kubelka-Munk transformation, which gives a slight blue shift relative to that of bulk C₃N₄ (~2.70 eV) because of the quantum confinement [24,25]. The UV-vis spectrum of CoO NP catalysts presents an absorption band edge at around 500 nm ascribed to ligand-metal charge transfer events O^{II}→Co^{II}. The other broad band edge at approximately 760 nm arises from Co(II) *d-d* transitions, implying that the Co²⁺ ions are tetrahedrally coordinated [26]. The spectrum of the CoO(7)/C₃N₄ NTs exhibits a new absorption broad edge at about 670 nm (enlarged in the inset part), compared with the bare C₃N₄ NTs, which can be attributed to the CoO component. This indicates that the loading of CoO NPs resulted in more visible-light response on the C₃N₄ NT-based material due to the synergistic effect between two semiconductors. The spectrum of the bare Co₃O₄ NPs shows two absorptions centered at around 330 and 650 nm, which are attributed to ligand-metal charge transfer between O^{II}→Co^{II} and O^{II}→Co^{III}, respectively [27,28]. As shown in Fig. 5b, the Co₃O₄/C₃N₄ NTs display very similar properties with two light absorptions at *ca.* 2.12 eV and *ca.* 2.46 eV, which presents combined behaviours from the Co₃O₄ and C₃N₄ NT materials.

To further explore the origin of the improved photocatalytic performance, the steady-state photoluminescence spectra of the nanocomposites are shown in Fig. 6a. The bare C₃N₄ NTs exhibit a broad PL emission band with a peak centered at approximately 460 nm, which matches well with our UV-vis DRS results, demonstrating that the C₃N₄ NT material can act as a blue light-emitting material [11,18]. Integrating C₃N₄ NTs with CoO NPs led to a decreased intensity compared to that with Co₃O₄ NPs. This indicates that the deposition of CoO on C₃N₄ NTs could greatly inhibit the recombination of photo-generated carriers. The PL spectra of CoO and Co₃O₄ NPs were much weaker than those of the two nanocomposites and C₃N₄ NTs. They exhibit negligible PL intensity. As shown in the inset of Fig. 6a, it can be seen that the PL intensity of CoO is slightly lower than that of Co₃O₄. This can be one of the reasons that CoO NPs exhibit better photocatalytic performance than Co₃O₄ as depicted in Fig. 1.

The lifetimes of the excited electrons on the nanocomposites were measured by the TCSPC technique. The average lifetimes of (9.47 ± 0.03) , (8.02 ± 0.04) , (7.60 ± 0.03) , (5.80 ± 0.03) and (5.63 ± 0.02) ns were obtained on CoO(7)/C₃N₄ NTs, Co₃O₄(7)/C₃N₄ NTs, C₃N₄ NTs, CoO and Co₃O₄, respectively. A longer lifetime of the

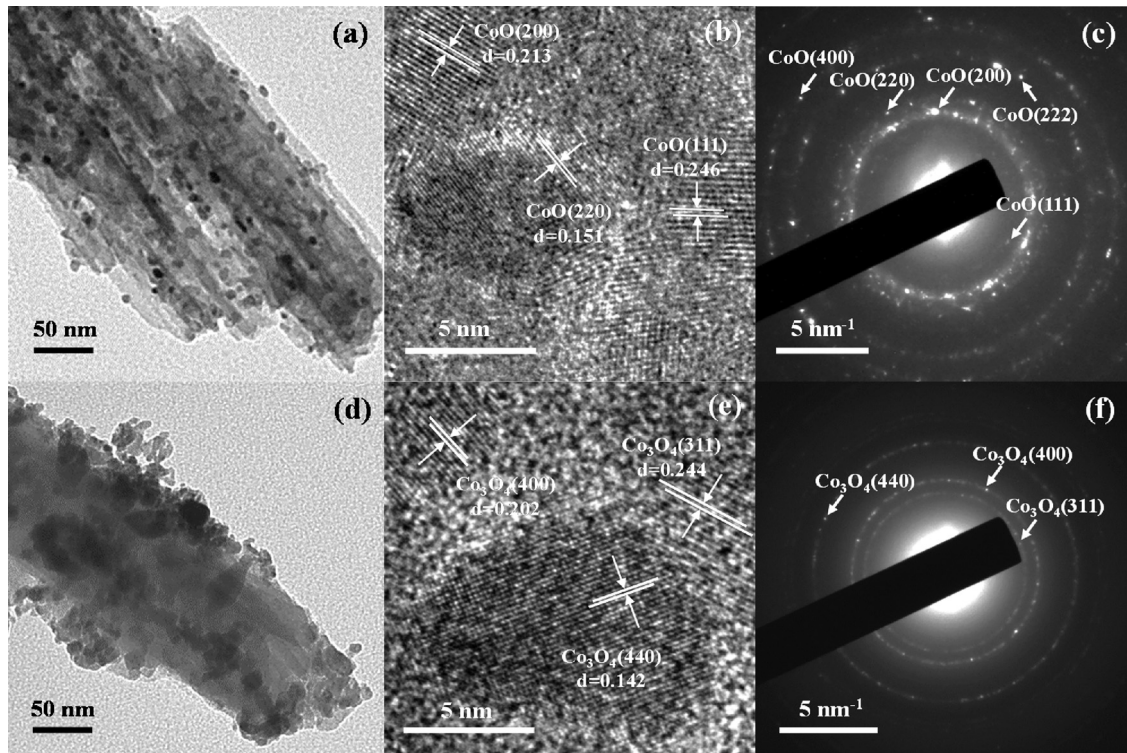


Fig. 4. TEM images of CoO(7)/C₃N₄ NT (a–c) and Co₃O₄(7)/C₃N₄ NT (d–f).

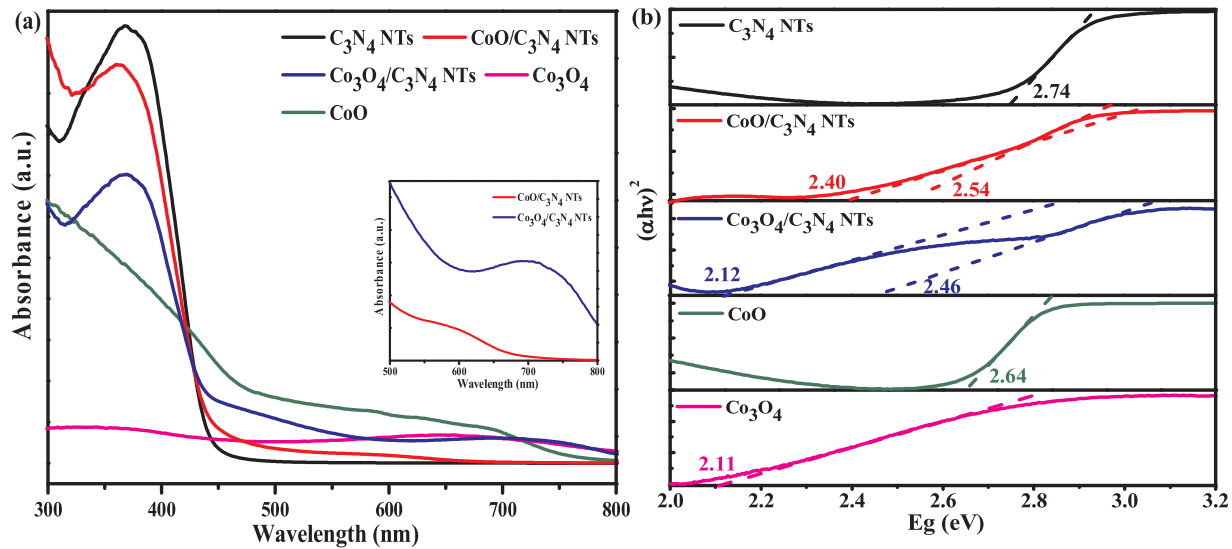


Fig. 5. UV-vis diffuse reflectance spectra of the photocatalysts studied in this work.

material generally means a greater opportunity of contributing more excited electrons to the semiconductor [29]. This finding also explains why CoO(7)/C₃N₄ NTs exhibit the best photocatalytic performance in hydrogen generation among all the materials studied in this work.

As shown in Fig. 7, the transient photocurrent responses of the samples were investigated by three on-off cycles of intermittent visible-light irradiation with good reproducibility. A considerably enhanced photocurrent was generated on CoO(7)/C₃N₄ NTs, about 1.6 times as high as that of Co₃O₄(7)/C₃N₄ NTs and higher than all the other nanomaterials present in this work. The sequence of photocurrent densities in order is CoO(7)/C₃N₄ NTs > Co₃O₄(7)/C₃N₄ NTs > C₃N₄ NTs > CoO > Co₃O₄. This result reveals that recombination of electron-hole pairs was greatly retarded and the separation of charge carriers at the interface between CoO and C₃N₄ NTs was improved. It

further confirms the above PL results. It is worth noting that the CoO(7)/C₃N₄ NTs performs higher stability than the Co₃O₄(7)/C₃N₄ NTs, agreeing with the stability test results depicted in Fig. 2. In comparison with Co₃O₄(7)/C₃N₄ NT nanocomposites, the higher stability of CoO(7)/C₃N₄ NTs may be attributed to the smaller CoO particle size and good dispersion along the channel of the tubes as confirmed in the TEM images.

The surface chemical compositions and oxidation states of the nanocomposites studied in this work were analyzed by XPS. The wide-scan XPS spectra implied that CoO/C₃N₄ NTs and Co₃O₄/C₃N₄ NTs consisted of C, N, Co and O elements (Fig. S6, Supporting Information). Based on the Co/N atom ratios determined by XPS, the CoO and Co₃O₄ content on the C₃N₄ NT surface were obtained, respectively, agreeing very well with the above SEM-EDS results. Fig. 8a–b show the Co 2p

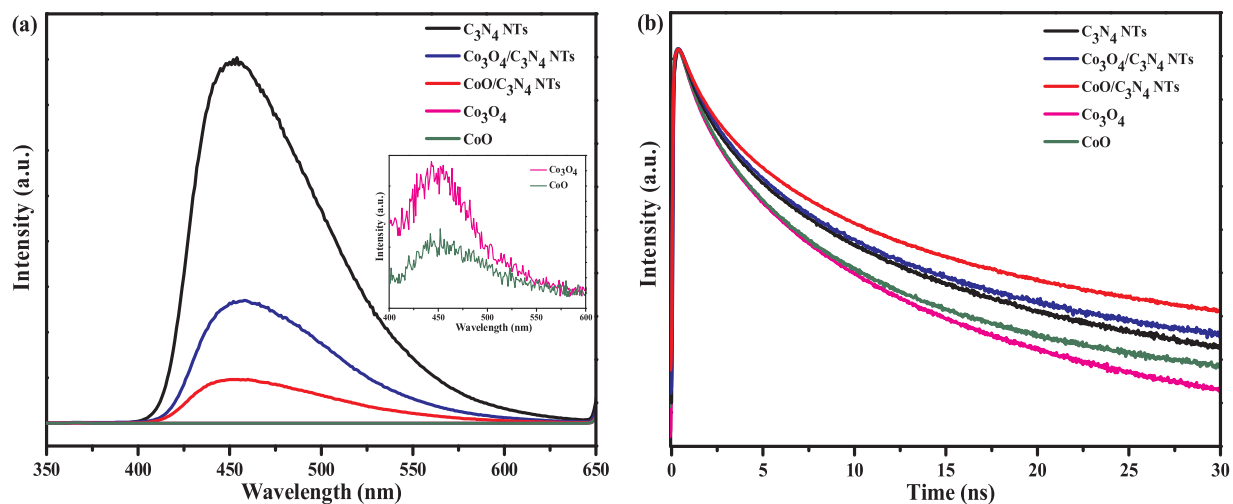


Fig. 6. Photoluminescence spectra (a) and transient decay curves (b) of the photocatalysts studied in this work.

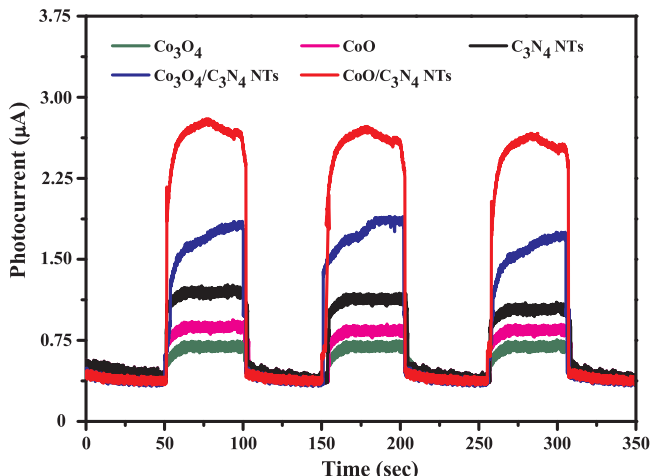


Fig. 7. The periodic on/off photocurrent response of the photocatalysts studied in this work.

XPS spectra of CoO_x NPs and $\text{CoO}_x(7)/\text{C}_3\text{N}_4$ NTs with peak fitting. In Fig. 8a, the binding energy at 780.5 and 796.1 eV is assigned to CoO $2p_{1/2}$ and $2p_{3/2}$ species on the surface of $\text{CoO}/\text{C}_3\text{N}_4$ NTs, respectively. The shake-up satellite structures apart from the main peaks verify the existence of Co(II) species [21,30], confirming the successful deposition of pure CoO . This is in line with the XRD and TEM results. Compared to the XPS spectrum of the bare CoO NPs, the CoO $2p_{1/2}$ and $2p_{3/2}$ peaks are slightly shifted toward a lower binding energy region, indicating a strong interaction between CoO and the underlying C_3N_4 NT support.

A similar phenomenon is also observed in the Co 2p XPS spectra of $\text{Co}_3\text{O}_4(7)/\text{C}_3\text{N}_4$ NT and Co_3O_4 samples as depicted in Fig. 8b. The Co 2p spectrum of Co_3O_4 NPs can be deconvoluted into one pair of shakeup satellites and two spin-orbit doublets. The Co 2p doublet at 779.9 and 794.9 eV are attributed to Co^{2+} species, while another at 781.9 and 796.2 eV belong to Co^{3+} species, which confirms the formation of Co_3O_4 phase [31]. For $\text{Co}_3\text{O}_4(7)/\text{C}_3\text{N}_4$ NTs, the peaks exhibit negative shifts. On the other hand, as shown in Fig. 8c, the N 1s XPS spectra of both $\text{CoO}(7)/\text{C}_3\text{N}_4$ NTs and $\text{Co}_3\text{O}_4(7)/\text{C}_3\text{N}_4$ NTs exhibit a positive shift as compared to the bare C_3N_4 NTs, indicating a strong interaction between Co and N atoms. He et al. reported that chemical bonds between ZnO and C_3N_4 were formed [32]. The larger shifts in Co 2p and N 1s XPS spectra were observed for $\text{CoO}(7)/\text{C}_3\text{N}_4$ NTs compared with that for $\text{Co}_3\text{O}_4(7)/\text{C}_3\text{N}_4$ NTs, implying stronger interaction between CoO and C_3N_4 NTs. The strong interaction between cobalt oxides and C_3N_4 NTs.

NT support is beneficial for the formation of heterojunctions, thus promoting a smooth charge transfer between the two semiconductors.

The VB XPS spectra as shown in Fig. 8d reveal that the VB potentials (E_{VB}) of CoO , Co_3O_4 , and C_3N_4 NTs are 1.44, 1.61 and 2.12 eV relative to the normal hydrogen electrode (NHE), respectively. These values are all more positive than the redox potential of $\text{O}_2/\text{H}_2\text{O}$ (1.23 eV vs NHE). Considering the band gap determined by the UV-vis DRS, the CB potentials (E_{CB}) of CoO , Co_3O_4 , and C_3N_4 NTs are located at -1.20 , -0.50 and -0.62 eV vs NHE, respectively, which are much more negative than the reduction potential of H^+/H_2 (-0.42 eV vs NHE). Therefore, the band structures of CoO , Co_3O_4 , and C_3N_4 NTs studied in this work are suitable for hydrogen production from water splitting. It is also noted that the CB and VB positions of CoO NPs, Co_3O_4 NPs and C_3N_4 NTs were upshifted in comparison with the bulk CoO [7], Co_3O_4 [28] and C_3N_4 [33]. Both of the CB band edges of CoO NPs and Co_3O_4 NPs are higher than the level of H^+/H_2 at -0.42 eV, which confirms the feasibility for H_2 generation.

To further verify the band edge potentials, the flat band potentials of C_3N_4 NTs, CoO NPs and Co_3O_4 NPs were recorded by the Mott-Schottky plots from electrochemical impedance spectroscopy. As shown in Fig. S7a (Supporting Information), the positive slope of the Mott-Schottky plot indicates that the C_3N_4 NT is an *n*-type semiconductor. The E_{CB} for *n*-type semiconductors is very close to the flat-band potential value, *i.e.*, E_{CB} of C_3N_4 NTs at *ca.* -0.83 eV *versus* Ag/AgCl (equivalent to -0.63 eV vs NHE). In the case of *p*-type semiconductors, E_{VB} is generally located near the flat-band potential [34]. Both CoO NPs and Co_3O_4 NPs exhibit a Mott-Schottky plot with negative slopes, suggesting that these cobalt oxides act as *p*-type semiconductors. Fig. S7b–c gives the E_{VB} of CoO and Co_3O_4 at *ca.* 1.24 eV and 1.41 eV, respectively (corresponding to 1.44 eV and 1.61 eV vs NHE). The results agree well with the above VB XPS and UV-vis DRS analysis.

3.3. Interpretation of charge transfer and reaction pathways

A schematic diagram proposing the photocatalytic hydrogen production process occurring on $\text{CoO}(7)/\text{C}_3\text{N}_4$ NT and $\text{Co}_3\text{O}_4(7)/\text{C}_3\text{N}_4$ NT heterojunctions is depicted in Fig. 9. Finer CoO NPs were more evenly distributed on the surface of C_3N_4 NTs, whereas Co_3O_4 in larger particle sizes were aggregated to some extent. On the basis of the above results, the CB edge of CoO is more negative than that of C_3N_4 NTs, while the VB level of C_3N_4 NTs is more positive than that of CoO . Upon visible-light irradiation (> 420 nm) CoO and C_3N_4 NTs can be activated simultaneously, and the excited electrons will immediately transfer from the VB to CB within the semiconductors. The electrons on the CB of the *p*-type CoO semiconductor will directly transfer to that of *n*-type C_3N_4 .

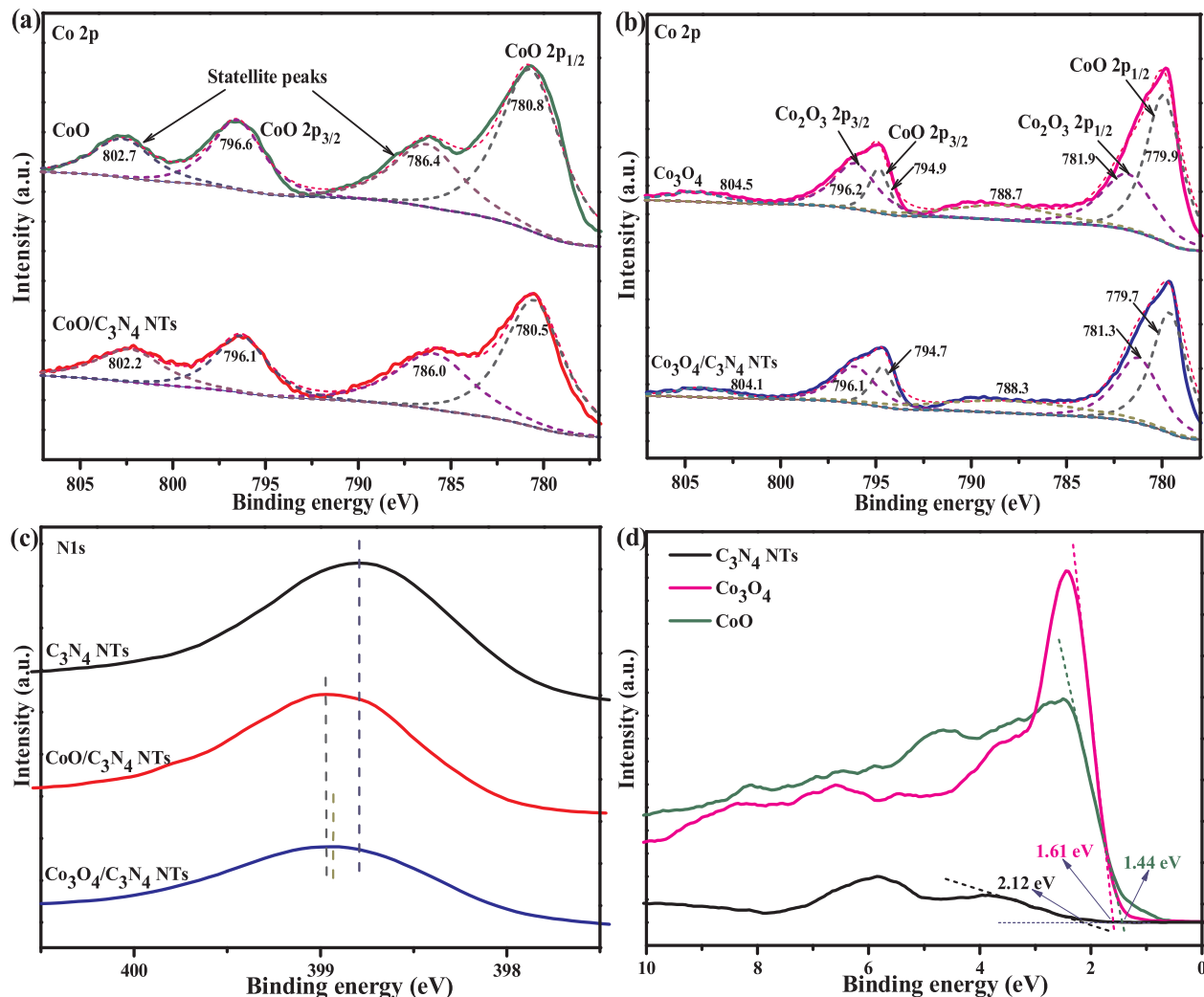


Fig. 8. Co 2p XPS spectra of CoO NPs and CoO(7)/C₃N₄ NTs (a), and Co₃O₄ NPs and Co₃O₄(7)/C₃N₄ NTs (b); N 1s XPS spectra of the bare C₃N₄ NTs and cobalt oxide modified samples (c); VB XPS of C₃N₄ NTs, CoO and Co₃O₄ NPs (d).

NTs, and the holes on the VB of C₃N₄ NTs can be spontaneously injected to that of CoO under the potential of the band energy difference. The migration of these photo-generated carriers can be promoted by the strongly interacting interface. As a result, the synergistic effect

between C₃N₄ NTs and CoO formed a staggered gap of Type II alignment [35]. The electrons at the CB of the semiconductors are able to reduce H₂O to H₂, whereas holes in the VB can be consumed through the oxidation of TEA to diethylamine (DEA) and acetaldehyde

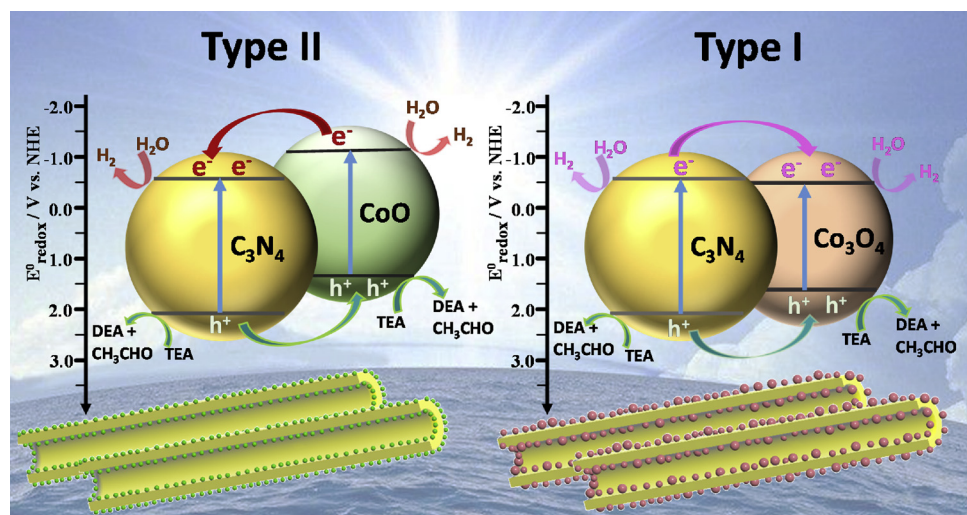


Fig. 9. Schematic illustration of the proposed mechanism in the tunable cobalt oxide/C₃N₄ NT heterojunction architectures.

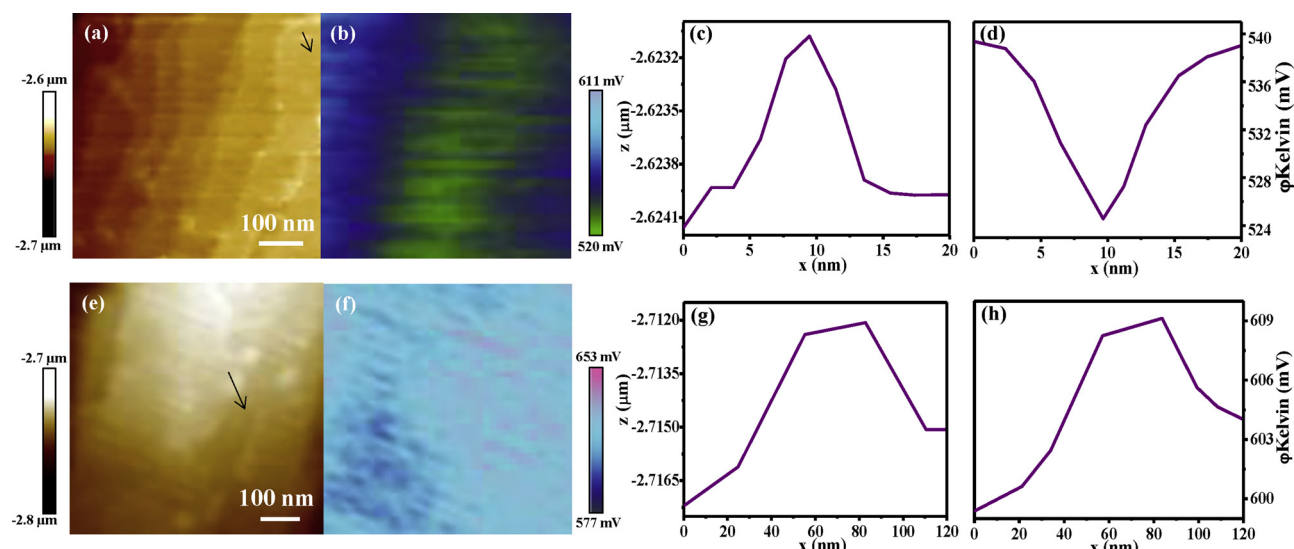


Fig. 10. Topography images, surface potentials, line-scanning profile through one cobalt oxide particle, and the corresponding Kelvin probe signals of CoO(7)/C₃N₄ NT (a–d) and Co₃O₄(7)/C₃N₄ NT (e–h).

spontaneously as we reported previously [5]. Compared to the recently reported CoO/C₃N₄ NS photocatalyst synthesized by solvothermal method, the photo-excited electrons transfer from C₃N₄ NSs to CoO, while the holes in the VB of CoO migrate to that of C₃N₄ NSs, which is due to the large particle size of anchored CoO NPs (10–20 nm) [15].

On the other hand, the CB edge of Co₃O₄ is lower than that of C₃N₄ NTs, and its VB position is above that of C₃N₄ NTs. When Co₃O₄(7)/C₃N₄ NTs are exposed to visible light, both Co₃O₄ and C₃N₄ NTs will be excited. The electrons on the CB of C₃N₄ NTs will quickly transfer to that of Co₃O₄, and the holes on the VB of the C₃N₄ NTs will simultaneously hop into that of Co₃O₄ as well. Therefore, the electrons and holes will accumulate in the Co₃O₄ semiconductor and recombine rapidly. Hence, Co₃O₄(7)/C₃N₄ NTs exhibit the Type I straddled band alignment [35]. Unlike the Type I, the Type II heterojunction provides the optimum band positions for separating charge carriers efficiently, hindering charge recombination significantly, and prolonging electron lifetimes, thus leading to enhanced photocatalytic activity.

To further verify the charge transfer pathways firstly proposed in this work, KPFM was conducted to obtain topography images and electrostatic potentials above the sample surface simultaneously. Fig. 10 shows the topography images, surface potentials, line-scanning profile through one cobalt oxide particle, and the corresponding Kelvin probe signals of CoO(7)/C₃N₄ NTs (a–d) and Co₃O₄(7)/C₃N₄ NTs (e–h), respectively. From Fig. 10a, small CoO NPs were observed on the surface of C₃N₄ NTs. The particle size of CoO is about 8 nm as depicted in the line-scanning profile through one CoO particle in Fig. 10c. Similar in the TEM images, the line scanning profile through one Co₃O₄ particle gives a particle size of around 50–80 nm as shown in Fig. 10g, confirming that CoO(7)/C₃N₄ NT sample exhibits finer CoO particle than Co₃O₄(7)/C₃N₄ NT. Moreover, it is observed that the surface electrical potential gradient of CoO(7)/C₃N₄ NTs (90 mV) is higher than that of Co₃O₄(7)/C₃N₄ NTs (76 mV), indicating stronger electronic interaction between CoO and C₃N₄ NTs. Hence, it is understandable that CoO(7)/C₃N₄ NTs exhibited an enhanced visible-light photocatalytic activity compared to Co₃O₄(7)/C₃N₄ NTs.

The Kelvin probe signal is defined as the electrostatic potential offset between a probe tip and the surface [36]. As shown in Fig. 10d, a negative Kelvin probe signal of around 14 mV corresponding to a positive electrostatic potential at the position of tip was observed on the surface of CoO(7)/C₃N₄ NT sample, implying a transfer of negative charges, *i.e.* electrons, from the CoO particle to the underlying C₃N₄ NT surface. On the other hand, a positive Kelvin probe signal of about 6 mV

was recorded on the surface of Co₃O₄(7)/C₃N₄ NT nanomaterials (Fig. 10h), which reflects a negative electrostatic potential at the position of tip and therefore indicates a transfer of electrons from the C₃N₄ NT support to the Co₃O₄ particle. These experimental evidences firmly verify the direction of charge transfer pathways as proposed in Fig. 9. It is worth mentioning that the electrostatic potential offset of CoO(7)/C₃N₄ NT (14 mV) is larger than that of Co₃O₄(7)/C₃N₄ NT sample (6 mV), further proving a higher driving force for electron transfer from CoO to C₃N₄ NTs than that from C₃N₄ NTs to Co₃O₄. Therefore, the Type II heterojunction coupling of CoO NPs with C₃N₄ NTs led to the improved hydrogen production performance.

4. Conclusion

The present work successfully designed tunable heterojunction architectures of CoO_x NPs confined on well-arrayed C₃N₄ NTs by using the same one-pot method under different annealing atmospheres. Annealing under vacuum condition ensured a Type II heterojunction with a good dispersion of CoO NPs with a particle size of less than 8 nm along the C₃N₄ NTs surface. Annealing under static air led to a Type I heterojunction of Co₃O₄/C₃N₄ NTs with an enlarged particle size of Co₃O₄ NPs up to a wide range of 20–80 nm and certain aggregation. These two heterojunctions present a distinct activity and stability in photocatalytic hydrogen production process. More specifically, CoO/C₃N₄ NTs with a CoO content of 7 wt. % exhibit the highest H₂ generation rate and the best stability compared with Co₃O₄/C₃N₄ NTs. The steady-state fluorescence and TCSPC technique confirm the fastest electron transfer between the conduction band of CoO and C₃N₄. According to the band edge potentials of the semiconductors determined in this work, CoO/C₃N₄ NT and Co₃O₄/C₃N₄ NT nanostructures are identified as Type II and Type I heterojunctions, respectively. Experimental evidences obtained from KPFM firmly verify the charge transfer pathways established in this work. This research provided a greater understanding of charge transfer pathways in different heterojunction architectures and identified the beneficial attributes to the efficient visible-light photocatalytic hydrogen production process.

Acknowledgements

We thank the Microscopy Unit at Macquarie University for TEM characterization. Financial support by the ARC Discovery Early Career Researcher Award (DE120100329), ARC Discovery Project

(DP140102432) and China Scholarship Council CSC scholarship for Y. Zhu is gratefully acknowledged. We are grateful to Prof. Emil Roduner from University of Stuttgart for his valuable comments on KPFM studies. We also thank Dr. Yin Yao for technical assistance and use of facilities at the Electron Microscope Unit at UNSW.

Appendix A. Supplementary data

Supplementary material related to this article can be found, in the online version, at doi:<https://doi.org/10.1016/j.apcatb.2018.12.015>.

References

- [1] W. Lubitz, W. Tumas, *Chem. Rev.* 107 (2007) 3900–3903.
- [2] A. Kudo, Y. Miseki, *Chem. Soc. Rev.* 38 (2009) 253–278.
- [3] Y. Li, P. Li, J. Wang, Y. Yang, W. Yao, Z. Wei, J. Wu, X. Yan, X. Xu, Y. Liu, Y. Zhu, *Appl. Catal. B: Environ.* 225 (2018) 519–529.
- [4] C. Zhou, R. Shi, L. Shang, L. Wu, C. Tung, T. Zhang, *Nano Res.* 11 (2018) 3462–3468.
- [5] Y. Zhu, A. Marianov, H. Xu, C. Lang, Y. Jiang, *ACS Appl. Mater. Int.* 10 (2018) 9468–9477.
- [6] F. Jiao, H. Frei, *Energy Environ. Sci.* 3 (2010) 1018–1027.
- [7] L. Liao, Q. Zhang, Z. Su, Z. Zhao, Y. Wang, Y. Li, X. Lu, D. Wei, G. Feng, Q. Yu, X. Cai, J. Zhao, Z. Ren, H. Fang, F. Robles-Hernandez, S. Baldelli, J. Bao, *Nat. Nanotechnol.* 9 (2014) 69–73.
- [8] X. Zhan, Z. Wang, F. Wang, Z. Cheng, K. Xu, Q. Wang, M. Saifdar, J. He, *Appl. Phys. Lett.* 105 (2014) 153903.
- [9] H.Q. Sun, H.M. Ang, M.O. Tade, S.B. Wang, *J. Mater. Chem. A* 1 (2013) 14427–14442.
- [10] A. Agiral, H.S. Soo, H. Frei, *Chem. Mater.* 25 (2013) 2264–2273.
- [11] A. Gasparotto, D. Barreca, D. Bekermann, A. Devi, R.A. Fischer, P. Fornasiero, V. Gombac, O.I. Lebedev, C. Maccato, T. Montini, G. Van Tendeloo, E. Tondello, *J. Am. Chem. Soc.* 133 (2011) 19362–19365.
- [12] W.J. Ong, L.L. Tan, Y.H. Ng, S.T. Yong, S.P. Chai, *Chem. Rev.* 116 (2016) 7159–7329.
- [13] S.J.A. Moniz, S.A. Shevlin, D.J. Martin, Z. Guo, J. Tang, *Energy Environ. Sci.* 8 (2015) 731–759.
- [14] Z. Mao, J. Chen, Y. Yang, D. Wang, L. Bie, B. Fahlman, *ACS Appl. Mater. Int.* 9 (2017) 12427–12435.
- [15] F. Guo, W. Shi, C. Zhu, H. Li, Z. Kang, *Appl. Catal. B: Environ.* 226 (2018) 412–420.
- [16] J. Zhang, M. Grzelczak, Y. Hou, K. Maeda, K. Domen, X. Fu, M. Antonietti, X. Wang, *Chem. Sci.* 3 (2012) 443–446.
- [17] C. Han, L. Ge, C. Chen, Y. Li, X. Xiao, Y. Zhang, L. Guo, *Appl. Catal. B: Environ.* 147 (2014) 546–553.
- [18] S. Wang, C. Li, T. Wang, P. Zhang, A. Li, J. Gong, *J. Mater. Chem. A* 2 (2014) 2885–2890.
- [19] G. Zhang, S. Zang, X. Wang, *ACS Catal.* 5 (2015) 941–947.
- [20] J. Yu, S. Wang, B. Cheng, Z. Lin, F. Huang, *Catal. Sci. Technol.* 3 (2013) 1782.
- [21] B. Liu, L. Ma, L. Ning, C. Zhang, G. Han, C. Pei, H. Zhao, S. Liu, H. Yang, *ACS Appl. Mater. Int.* 7 (2015) 6109–6117.
- [22] C. Peng, B. Chen, Y. Qin, S. Yang, C. Li, Y. Zuo, S. Liu, J. Yang, *ACS Nano* 6 (2012) 1074–1081.
- [23] Y. Mao, W. Li, P. Liu, J. Chen, E. Liang, *Mater. Lett.* 134 (2014) 276–280.
- [24] Z. Khan, M. Khannam, N. Vinothkumar, M. De, M. Qureshi, *J. Mater. Chem.* 22 (2012) 12090.
- [25] Z. Jin, Q. Zhang, S. Yuan, T. Ohno, *RSC Adv.* 5 (2015) 4026–4029.
- [26] D.S. Negi, B. Loukyka, K. Dileep, R. Sahu, K.K. Nagaraja, N. Kumar, R. Datta, *Appl. Phys. Lett.* 103 (2013) 242407.
- [27] C. Tang, E. Liu, J. Wan, X. Hu, J. Fan, *Appl. Catal. B: Environ.* 181 (2016) 707–715.
- [28] M. Long, W. Cai, J. Cai, B. Zhou, X. Chai, Y. Wu, *J. Phys. Chem. B* 110 (2006) 20211–20216.
- [29] N.M. Tzallas, G.A. Zachariadis, A.N. Anthemidis, J.A. Stratis, *Int. J. Environ. Anal. Chem.* 90 (2010) 115–126.
- [30] D. Gallant, M. Pezolet, S. Simard, *J. Phys. Chem. B* 110 (2006) 6871–6880.
- [31] X. Wang, Y. Zheng, J. Yuan, J. Shen, A.-j. Wang, L. Niu, S. Huang, *Electrochim. Acta* 212 (2016) 890–897.
- [32] Y. He, Y. Wang, L. Zhang, B. Teng, M. Fan, *Appl. Catal. B: Environ.* 168–169 (2015) 1–8.
- [33] H. Huang, K. Xiao, N. Tian, F. Dong, T. Zhang, X. Du, Y. Zhang, *J. Mater. Chem. A* 5 (2017) 17452–17463.
- [34] L. Zhang, Y. Hu, J. Zheng, *J. Mater. Chem. A* 5 (2017) 18664–18673.
- [35] R. Marschall, *Adv. Funct. Mater.* 24 (2014) 2421–2440.
- [36] T. Kittel, E. Roduner, *J. Phys. Chem. C* 120 (2016) 8907–8916.